PAPER

Check for updates

Fundamental insight into enhanced activity of Pd/CeO2 thin films in hydrogen oxidation reaction in alkaline media†

Mathilde Luneau, [ID] *[ab] Linnéa Strandberg, [ID] [b] Gerard Montserrat-Sisó, [ID] [b] Victor Shokhen, [ID] [b] Roopathy Mohan,[b] Henrik Grönbeck [ID] [b] and Björn Wickman [ID] [b]

Palladium supported on ceria (Pd/CeO2) has recently raised strong interest as an alternative catalyst to platinum on the anode electrode in anion exchange membrane fuel cells. Herein, we provide new insight into the enhanced activity of Pd/CeO2 in hydrogen oxidation reaction (HOR) in alkaline media. Using well-defined model thin films, we show that Pd/CeO2 thin films lead to enhanced activity in HOR compared to pure Pd thin films. *In situ* characterization using electrochemical quartz crystal microbalance provide in-depth understanding of the role of CeO2. CeO2 leads to fundamental differences in adsorption and absorption of key reaction intermediates during HOR. In combination with characterization and theoretical calculations, Pd atoms embedded in CeO2 are shown to be present on the prepared thin films and active for hydrogen activation but are not able to bind CO during CO-stripping characterization. Finally, an estimation of the source of hydroxyl intermediates provided by CeO2 – which could be directly participating in the reaction – is presented herein. Fundamental understanding of the Pd–CeO2 interface in HOR opens new ways to reduce the amount of noble metals in alkaline fuel cells.

aDepartment of Chemistry and Chemical Engineering, Competence Centre for Catalysis, Chalmers University of Technology, Gothenburg, SE 41296, Sweden. E-mail: mathilde.luneau@chalmers.se

bDepartment of Physics, Competence Centre for Catalysis, Chalmers University of Technology, Gothenburg, SE 41296, Sweden

† Electronic supplementary information (ESI) available. See DOI: https://doi.org/10.1039/d3ta01879b

Dr Mathilde Luneau is an Assistant Professor at the Department of Chemistry and Chemical Engineering at Chalmers University of Technology in Gothenburg, Sweden. Before joining Chalmers University of Technology, she was a postdoctoral fellow at Harvard University, USA in the group of Prof. Cynthia Friend. Mathilde obtained her PhD from the University of Lyon 1, France in 2016 where she worked at the Institute of Research on Catalysis and Environment (IRCELyon). Her research focuses on the design and understanding of novel catalytic materials for applications in electrocatalytic and thermocatalytic reactions.

Introduction

Demand for non-fossil fuel-based electricity is growing rapidly and conversion of hydrogen into electricity in fuel cells has received increasing interest in the past decades. The most common fuel cell is presently the proton-exchange membrane fuel cell (PEMFC). One drawback with PEMFCs is, however, the use of Pt-based catalysts. Pt-based catalysts are required to achieve a high activity for the fuel cell reactions and to withstand the harsh acidic conditions and varying electric potential over long periods of operation. The high cost associated with scarce Pt-based catalysts is limiting the use of fuel cells. To remedy this problem, anion-exchange membrane fuel cells (AEMFCs) have gained interest in recent years.[1] The high pH in AEMFCs allows the use of alternative Pt-free catalysts although the reaction rate of the hydrogen oxidation reaction (HOR) in alkaline media is orders of magnitude lower than in acidic conditions.[2] Catalytic materials with enhanced HOR activity in alkaline media must thus be designed. A promising approach is to design catalysts with strong metal–support interfaces.

Recently, CeO2 has been used as a support for Pd in AEMFC applications and it was proposed that the Pd/CeO2 metal–support interface plays a prominent role in the improved activity.[3,4] While Pd–PdO catalysts have shown good performance in various electrochemical reactions such as CO2 electroreduction and methanol electrooxidation, they have poor activity for HOR.[5–7] The promotion of Pd catalysts by supports

16370 | *J. Mater. Chem. A*, 2023, **11**, 16370–16382

This journal is © The Royal Society of Chemistry 2023

such as ceria has however led to significant enhancement in HOR. The metal-support interface dynamics have been shown to affect performance in heterogeneous catalysis.[8] Their understanding and modulation can thus lead to important enhancement in activity. These interactions have been shown to drive catalytic activity and to be most impactful for dispersed single metal atoms and nanoparticles smaller than *ca.* 4 nm.[9,10] In recent years, most efforts have been put on establishing strategies to best utilize, tune and maximize these interactions to enhance activity. Due to the diversity of possible metal–support combinations and interactions, the interface dynamics have been investigated for a wide range of applications.

In particular, the special synergy between precious metals and ceria (CeO_2) has raised a lot of attention in the past decades.[11,12] Ceria is known to act as an "oxygen storage" material with the ability to gain and release oxygen as Ce oxidation state changes between Ce^{4+} and Ce^{3+}. In industrial applications, this oxygen storage capability has been utilized in the automotive three way catalysts where CeO_2 is used as a promoter to remove pollutants originating from the combustion of gasoline.[13] The rare earth metal Ce, either used as a support in CeO_2 or as atomically dispersed species, has also led to significant enhancement in electrocatalytic applications and reactions, such as in oxygen evolution reaction, oxygen reduction reaction and in solid oxide fuel cells.[11,14–16] These beneficial interactions between precious metals and ceria have mainly been understood in terms of strong metal–support interaction, unique redox properties of CeO_2, electronic interaction between the metal and the metal oxide, and hydrogen spillover.[17]

In alkaline media, HOR has been suggested to proceed *via* two main mechanisms: (i) the Tafel–Volmer pathway (combining eqn (1) and (3)) or (ii) the Heyrovsky–Volmer pathway (combining eqn (2) and (3)):

$$H_2 + 2* \rightleftharpoons 2H*, \text{Tafel reaction} \quad (1)$$

$$H_2 + OH^- +* \rightleftharpoons H* + H_2O + e^-, \text{Heyrovsky reaction} \quad (2)$$

$$H* + OH^- \rightleftharpoons * + H_2O + e^-, \text{Volmer reaction} \quad (3)$$
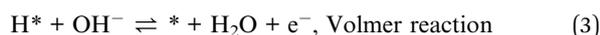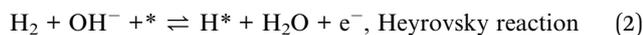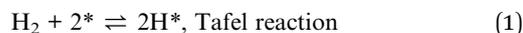
where * stands for an active site and H* stands for adsorbed hydrogen.

The hydrogen binding energy is often used as a descriptor for hydrogen evolution and oxidation reactions.[18] In a so-called volcano plot, the logarithm of the exchange current density in alkaline media was correlated with the calculated hydrogen binding energy (H-BE) on metal surfaces, with Pt near the top.[19] In this interpretation, weak hydrogen binding results in a slow Volmer step, limiting the overall rate. Strong hydrogen binding (such as on Pd) leads to a competition between adsorption and desorption which limits the Tafel step. Following the Sabatier principle, an ideal catalyst must bind the hydrogen atoms not too strongly and not too weakly.

In alkaline media, adsorbed hydroxyl groups can also play an important role in the reaction.[20,21] Adsorbed OH groups are traditionally considered as spectators or inhibiting species.[22]

OH adsorption ($OH^- + * \rightleftharpoons OH* + e^-$) can inhibit H_2 adsorption and dissociation if OH binds too strongly and if they compete for the same active sites. However, in alkaline media, OH groups have also been shown to play a promoting role in HOR.[20,21] Notably, a bifunctional effect was suggested to occur on PtRu catalyst and led to enhanced HOR activity compared to pure Pt.[20] The authors proposed that adsorbed OH groups on oxyphilic Ru could react with hydrogen intermediates adsorbed on nearby Pt sites. Therefore, both H and OH adsorption strengths must be considered in alkaline media.[23]

In addition to its oxygen storage capability, CeO_2 also has the ability to interact with hydrogen, in two different ways: one through the hydroxylation of the surface oxide and the second through the incorporation of hydrogen into the ceria lattice.[24] Surface hydroxyl groups are thus expected to play an important role in the reaction. In different applications such as steam reforming of ethanol, studies have shown that in the presence of water, CeO_2 participated in reactions by dissociating water and providing hydroxyl groups that can react.[25] Modified hydrogen interactions and hydroxyl groups participation in the reaction mechanism are thus important parameters that can influence the reactivity of Pd/CeO_2 catalysts.

A recent theoretical study investigated the Tafel–Volmer pathway for HOR on Pd/CeO_2 in alkaline media.[26] The authors attributed the catalytic improvement to a balance between the H and OH adsorption strengths and the strong interaction between Pd and the ceria support. Importantly, isolated Pd atoms on CeO_2 were suggested to lead to better performances than Pd clusters and were suggested to be the active sites. Looking at the Tafel step, isolated Pd atoms on CeO_2 were calculated to have comparable dissociation energy (DE) than Pd(111) (H_2-DE = 0.05 *vs.* 0.03 eV, respectively). The authors reported a stronger binding of hydrogen – *i.e.* more negative binding energy (BE) – on isolated Pd atoms on CeO_2 compared to extended Pd(111) surface (H-BE = −1.29 eV *vs.* −0.69 eV, respectively). In the Volmer step, the hydroxyl intermediate formed by adsorbing OH^- reacts with the dissociated hydrogen. On isolated Pd atoms on CeO_2, OH groups were found to bind less strongly than on extended Pd(111) surfaces (OH-BE = −3.25 eV *vs.* −3.33 eV). One important finding is that OH* was calculated to be able to bind to cerium, with H adsorbed on isolated Pd atoms, leading to an interface between Pd and Ce. Further understanding is still needed to elucidate the role of CeO_2 in the reaction.

Here we study model Pd/CeO_2 thin films with well-defined compositions and structures to gain fundamental understanding of the metal–metal oxide interface and its influence on HOR activity in alkaline media. Model thin films are ideal systems to study the fundamental metal/ceria interactions and have not yet been employed for HOR on Pd/CeO_2 in alkaline media. We develop an approach combining electrochemical measurements, *in situ* electrochemical characterization, *ex situ* microscopy and spectroscopy, and theoretical calculations to describe the interactions between Pd and CeO_2.

A key aspect of our study is the use of electrochemical quartz crystal microbalance (E-QCM) analysis. E-QCM is a powerful *in situ* technique generally used to evaluate the

This journal is © The Royal Society of Chemistry 2023

J. Mater. Chem. A, 2023, **11**, 16370–16382 | **16371**

stability of materials.[27] It is also a powerful method to investigate and quantify mass changes occurring on surfaces due to phenomena of dissolution, adsorption, absorption, physisorption and desorption, while the reaction is occurring.[28] Using E-QCM, we provide fundamental understanding of the adsorption, absorption and desorption phenomena occurring on Pd/CeO$_2$ thin films during HOR. We show that on pure Pd thin films, mass changes are dominated by the absorption of hydrogen while on Pd/CeO$_2$ they are dominated by the oxidation/reduction of ceria and adsorption of hydroxyl groups. One of the hypotheses for enhanced reactivity of Pd/CeO$_2$ in HOR is that CeO$_2$ – at the interface with Pd – serves as a source of OH groups which react with adsorbed H to form water.[29] In this study, we provide quantitative evidence that this hypothesis is valid using an *in situ* technique on model thin films.

Methods

Thin films were synthesized *via* electron-beam physical vapor deposition (AVAC HVC600) on glassy-carbon electrodes. Prior to deposition, the electrodes (5 mm diameter, Sigradur® disks from HTW GmbH) were cleaned by sequential sonication in acetone (Sigma-Aldrich), isopropanol (VWR) and Milli-Q water (18.2 MΩ cm) for 10 minutes each, and dried with N$_2$ (Grade N6.0, Strandmöllen) followed by plasma cleaning in O$_2$ atmosphere at 100 W for 1 minute. After cleaning, a 20 nm Ti underlayer was evaporated first to improve adhesion properties of Pd films to the electrodes. So-called pure Pd samples were prepared by evaporating 40 nm Pd thin films on the Ti adhesion layer. Pd/CeO$_2$ samples were prepared by evaporating a 20 nm CeO$_2$ film followed by a 2 nm Pd film. The electrodes have a geometrical surface area of 0.196 cm^2.

Electrochemical activity was studied using cyclic voltammetry (CV) in a standard three-electrode electrochemical cell in a rotating disk electrode (RDE) configuration (Pine Research Instrumentation). CVs were measured in 0.1 M KOH electrolyte in a polytetrafluoroethylene (PTFE) cell at room temperature using a graphite rod as counter electrode and a Hg/HgO reference electrode. All potentials in this study are reported *versus* the reversible hydrogen electrode (RHE) which were determined using a Pt counter electrode and a Pt working electrode while flowing H$_2$. Conditioning was performed in Ar by cycling at 100 mV s^{-1} for 20 cycles followed by 10 cycles at 50 mV s^{-1}. Hydrogen oxidation reaction was performed in H$_2$ by cycling at 5 mV s^{-1} and rotating at 1600 rpm. In another set of experiments, the rotation rate was varied between 400, 900, 1600 and 2500 rpm while cycling at 50 mV s^{-1} in H$_2$ after conditioning to obtain Koutecky–Levich plots. The cells were cleaned thoroughly with a piranha solution (3 : 1 ratio of concentrated sulfuric acid to 30% hydrogen peroxide solution) and rinsed with Milli-Q water between experiments. To further limit contamination, two cells were used: one for Pd-based samples and one for CeO$_2$ only.

The Koutecky–Levich equation was used to estimate the number of transferred electrons (n):

$$\frac{1}{j} = \frac{1}{j_k} + \frac{1}{j_{lim}} = \frac{1}{j_k} + \frac{1}{B\omega^{1/2}} \quad (4)$$

where $B = 0.2nFD_{H_2}^{2/3}\nu^{-1/6}C_{H_2}$, and where j is the current density, j_k is the kinetic current density, j_{lim} is the diffusion-limited current density, ω is the rotation rate in rpm, F is the Faraday constant (96 485 C mol^{-1}), D_{H_2} is the diffusion coefficient of H$_2$ in water (4.58×10^{-5} cm^2 s^{-1} at 20 °C),[30] ν is the kinematic viscosity (0.01 cm^2 s^{-1})[30] and C_{H_2} is the bulk concentration of H$_2$ in the solution (1×10^{-6} mol cm^{-3}).[31] The constant 0.2 is used as the rotation rate is in rpm.[23] The Koutecky–Levich plots were plotted using current densities measured at 0.8 V$_{RHE}$. This potential was chosen as it corresponds to the diffusion-limited region on both samples. At lower potentials, samples were not limited by the same phenomena (*i.e.* kinetic *vs.* diffusion).

Mass changes related to adsorption, absorption, physisorption or desorption phenomena were evaluated *in situ* with electrochemical-quartz crystal microbalance (Fig. 1). E-QCM measurements were performed on quartz crystals. The backside of the quartz crystals was precoated with Au on a Ti adhesion layer (Biolin Scientific). The crystals were first cleaned by sequential sonication in acetone, isopropanol and Milli-Q water for 10 minutes each, and dried in N$_2$ (Grade N6.0,
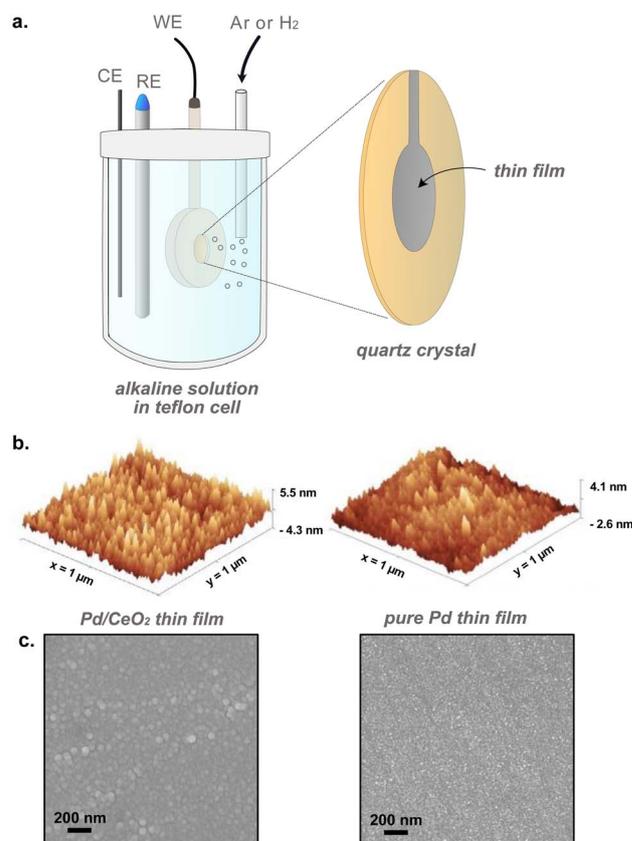
Fig. 1 (a) Schematic showing the setup used for *in situ* electrochemical characterization of thin films using E-QCM. RE, CE and WE refer to reference, counter and working electrodes, respectively. (b) Atomic force microscopy and (c) scanning electron microscopy images of Pd/CeO$_2$ and pure Pd thin films prepared by evaporation.

16372 | *J. Mater. Chem. A*, 2023, **11**, 16370–16382

This journal is © The Royal Society of Chemistry 2023

Strandmöllen) as a final step. Thin films of Pd and Pd/CeO$_2$ were evaporated on the crystals: (i) 20 nm Pd thin film on a 20 nm Ti adhesion layer for pure Pd samples, (ii) 2 nm Pd on 20 nm CeO$_2$ on a 20 nm Ti adhesion layer for the Pd/CeO$_2$ samples (Fig. 1b and c). Pd/CeO$_2$ was deposited on a Au thin layer to improve conductivity. The pure Pd thin films were conductive enough and did not require the use of a Au layer. The Pd and Pd/CeO$_2$ crystals have a geometrical surface area of 0.227 cm^2. In addition to these crystals, two control samples were prepared: (i) 20 nm CeO$_2$ on a Ti adhesion layer and (ii) Pd 2 nm on a Ti adhesion layer.

The E-QCM measurements were performed using a dip holder from MicroVacuum connected to a QSense Explorer frequency response analyzer (Biolin Scientific) with an in-house built adapter. The QCM data was recorded with the QSoft401 software (Biolin Scientific). The dip holder was made of PEEK, sealed using FFPM O-rings and assembled using nylon screws. The CV and frequency response were measured simultaneously on the same crystal.

The quartz crystal resonant frequency change Δf_n at different harmonic or overtone can be related to the mass change Δm using the Sauerbrey equation, assuming a spatially uniform film[32] (eqn (5)):

$$\Delta m = -\frac{A\sqrt{\rho_Q \mu_Q}}{2nf_0^2}\Delta f_n \tag{5}$$

where f_0 is the resonant frequency of the fundamental mode of the quartz crystal (ca. 4.95 MHz), n is the overtone number (7, 9 or 11 in our case), A is the piezoelectrically active area, ρ_Q is the density of quartz (2.648 g cm^{-3}), and μ_Q is the shear modulus of quartz (2.947 $\times$ 10^{11} g cm^{-1} s^{-2}). A constant $\Delta f_n/n$ when $n > 3$ ensures the validity of the Sauerbrey equation and confirms that the film can be considered as rigid.[33] During experiments, we measured the 7th, 9th and 11th overtones and made sure that $\Delta f_n/n$ was constant before further analysis. To further evaluate rigidity, dissipation was monitored during the experiment to differentiate mass loss from changes in surface roughness.[34]

In our system, a 1 Hz change in frequency corresponds to around ~2 ng cm$_{geo}^{-2}$ change in mass. Previous work done on 200 nm Pd film has however shown that the mass of hydrogen absorbed inside pure Pd bulk cannot be estimated with high accuracy due to additional frequency shifts attributed to the stresses generated when H-atoms diffuses into Pd.[35] Therefore, we plot Δf instead of Δm for clarity purposes, and make quantitative estimations related to mass changes only when away from the hydrogen absorption region ($E_{RHE} > 0.3$ V).

Electrochemically active surface area (ECSA) was assessed to provide a comparison between the very well defined pure Pd and Pd/CeO$_2$ films. Two different methods were used here to estimate their ECSAs: one derived from the charge required to oxidize a monolayer of adsorbed CO (CO-stripping method) and one derived from the charge resulting from the reduction of Pd oxide and/or hydroxide. Estimations using the charge related to hydrogen underpotential deposition is not appropriate in the case of Pd films as the H adsorption process is also coupled with an absorption of H into the Pd lattice, rendering estimations inaccurate.[36]

CO-stripping was performed by dosing CO in the electrolyte at 0.1 V$_{RHE}$ for 10 min and re-saturating with Ar for 30 min. The potential was then increased to 1.2 V$_{RHE}$ with a scan rate of 20 mV s^{-1} and cycled again to subtract the oxidation charge in the first positive-going scan associated with CO adsorbed on Pd, by the second scan corresponding to a CO-free surface. The ECSA was estimated by using a conversion charge of 330 μC cm$_{Pd}^{-2}$.[36] Estimations using the Pd oxide reduction method were done by integrating the charge in the last CV performed during conditioning, right before the HOR reaction, at a scan rate of 50 mV s^{-1} and with an inversion potential $E_{inversion} =$ 1.25 V$_{RHE}$. The corresponding ECSA was estimated using a conversion charge of 375 μC cm$_{Pd}^{-2}$.[36]

The structure of the thin films and sensors were probed using scanning electron microscopy (SEM – ZEISS Ultra-55 Scanning Electron Microscope). High-resolution transmission electron microscopy (HRTEM – FEI Titan operated at 300 kV) images were acquired on TEM grids (lacey carbon golden grids, Ted Pella, Inc.) onto which 20 nm of CeO$_2$ and 2 nm of Pd were evaporated. Atomic force microscopy (AFM) images were acquired using a Bruker dimension 3100 scanning probe microscope (SPM). Chemical composition of the surface species was assessed with X-ray photoelectron spectroscopy (XPS) with a PHI 5000 VersaProbe III spectrometer equipped with a monochromatic AlKα source. Narrow scan measurements were acquired with dual charge compensation and aligned with the adventitious carbon peak (C 1s) at 284.8 eV before analysis. Wide-angle X-ray scattering (WAXS) patterns in grazing incidence were acquired using the SAXSLAB Mat:Nordic instrument equipped with a micro-focus Cu X-ray source and a Dectris Pilatus 300 K R and 100 R detectors. The entire beam path was evacuated before each measurement to 0.5 mbar to minimize air scattering. The sample to detector distance was calibrated before each series of measurements using LaB$_6$. Exposure times were set to 6 hours per sample. Incidence angle of 0.4° was chosen to maximize the signal from the top layer. WAXS data was collected on the 100 R detector mounted on a goniometer inside of the evacuated chamber. Data reduction was performed using the SAXSgui software. Phase matching was performed using Bruker EVA software with the PDF + 2023 database.

Density functional theory (DFT) calculations were performed to gain insight into the oxidation state and structure of Pd on prepared Pd/CeO$_2$ thin films. The calculations were done using the Vienna Ab initio Simulation Package[37-40] using an approach described elsewhere.[41] The core–valence interaction was described with the plane augmented wave (PAW) method,[42] the Perdew, Burke and Ernzerhof (PBE) exchange–correlation functional[43] was used together with a Hubbard-U correction.[44] The Kohn–Sham orbitals are expanded with plane waves using a 450 eV cut-off. The atomic structures were optimized with the conjugate gradient method. A 3 $\times$ 2$\sqrt{3}$ surface cell was used for CeO$_2$(111) and the Brillouin zone sampling was restricted to the gamma point. The slabs are in all cases separated by at least 15 Å of vacuum. The core level shifts were calculated accounting for complete screening of the core hole.[41] The use of periodic boundary conditions requires a neutral supercell and we have

This journal is © The Royal Society of Chemistry 2023

J. Mater. Chem. A, 2023, **11**, 16370–16382 | **16373**

compensated the presence of core holes by a compensating jellium background.[45]

Results and discussion

Electrochemical characterization on glassy-carbon electrodes

Electrochemical characterization of Pd and Pd/CeO$_2$ films on glassy-carbon electrodes in the RDE set-up shows that the two systems have fundamentally different interactions with hydrogen. The CV profile performed in Ar-saturated 0.1 M KOH solutions on pure Pd is consistent with previously reported Pd thin films in alkaline solutions (Fig. 2a).[23] Pd and Pd/CeO$_2$ show very distinct potentials for hydrogen desorption. Hydrogen desorption/oxidation occurs from 0.0 to 0.4 V$_{RHE}$ (anodic peak) on Pd while it occurs from 0.0 to *ca.* 0.15 V$_{RHE}$ on Pd/CeO$_2$. Hydrogen absorption seems more pronounced on Pd compared to Pd/CeO$_2$. On Pd, there is a sharp cathodic peak starting from 0.2 until 0.0 V$_{RHE}$ which can be associated with hydrogen absorption into the Pd lattice to form Pd hydride. On Pd/CeO$_2$, this process only occurs from *ca.* 0.05 V$_{RHE}$.

Pd oxide species appear to be different on pure Pd compared to Pd/CeO$_2$. This is deduced from the difference in Pd surface oxides/hydroxides reduction potentials (Fig. 2a) with cathodic peaks at 0.75 V$_{RHE}$ and 0.67 V$_{RHE}$ on Pd and Pd/CeO$_2$ respectively. On pure Pd, the reduction of the Pd oxide can proceed *via*: $Pd-O + H_2O + 2e^- \rightarrow Pd + 2OH^-$. However, this reaction will be affected by the distribution and local coordination of Pd. Extended Pd surfaces on pure Pd thin films are thus expected to show different reduction peaks compared with Pd at the interface with ceria (including embedded Pd). This suggests that ceria not only impacts hydrogen interactions but also oxygen species.

Hydrogen oxidation is significantly enhanced on Pd/CeO$_2$ compared to pure Pd (Fig. 2b and c). In H$_2$-saturated KOH solution, the diffusion-limited current plateau is reached at 0.6 V$_{RHE}$ on pure Pd which is consistent with previous literature.[7,46] On Pd/CeO$_2$ that plateau is reached at a much lower potential of 0.4 V$_{RHE}$. The slightly lower diffusion-limited current density on Pd/CeO$_2$ could be due to limited leaching/pealing off of small amounts of Pd/CeO$_2$ active sites during rotation at 1600 rpm. Moreover, from 0 to 0.15 V$_{RHE}$, no measurable current is observed on pure Pd which could indicate that the Tafel step (step that does not involve charge transfer) is dominating in this potential range. The enhancement is demonstrated by a *ca.* 40-fold increase in specific activity at 0.1 V$_{RHE}$ on Pd/CeO$_2$ compared to Pd (Fig. 2c) which is consistent with other published work (Table S2†).[46] It should also be noted that there is an important anodic peak at 0.75 V$_{RHE}$ on pure Pd with a current significantly above the diffusion-limited current (Fig. 2b). This suggests that another reaction is occurring, notably the oxidation of hydrogen atoms absorbed in the Pd bulk.[36] Such high current peak is however not present on Pd/CeO$_2$ confirming that the presence of CeO$_2$ and the lower film thickness (2 nm *vs.* 20 nm for Pd/CeO$_2$ and pure Pd thin films respectively) lead to significant changes in the interaction with hydrogen (Fig. 2b).

Pd and Pd/CeO$_2$ present similar Tafel slopes (Fig. 3a). The Tafel slopes are 139 ± 5 and 135 ± 5 mV dec^{-1} respectively, close to 120 mV dec^{-1}. A value close to 120 mV dec^{-1} can be attributed to various reaction mechanisms (notably Tafel–Volmer) but it cannot be solely used to identify the rate determining step.[47] These values are however consistent with previously reported values for Pd/CeO$_2$-based catalysts in KOH solution.[3]

Both samples appear to present first order kinetics with respect to hydrogen as shown by the Koutecky–Levich plots (Fig. 3b) but present important dissimilarities. Pd/CeO$_2$ displays a linear behavior but does not intercept at the origin. This means that at this potential (0.8 V$_{RHE}$), the process is not purely diffusion-controlled. The number of transferred electron is estimated to be 2 which is expected for this reaction. Pure Pd, in turn, shows a close to zero intercept which means that the current is almost exclusively diffusion-limited at this potential. However, the number of transferred electrons is closer to 1. This deviation could be related to the interference of hydrogen absorbed into the Pd bulk, rendering the accurate estimation of transferred electrons difficult.[36]

New insights from E-QCM during conditioning

E-QCM measurements were performed to gain new insight into the role of CeO$_2$ at the interface with Pd. The CV obtained with a scan rate of 50 mV s^{-1} during conditioning in Ar saturated solution while measuring the frequency changes are consistent
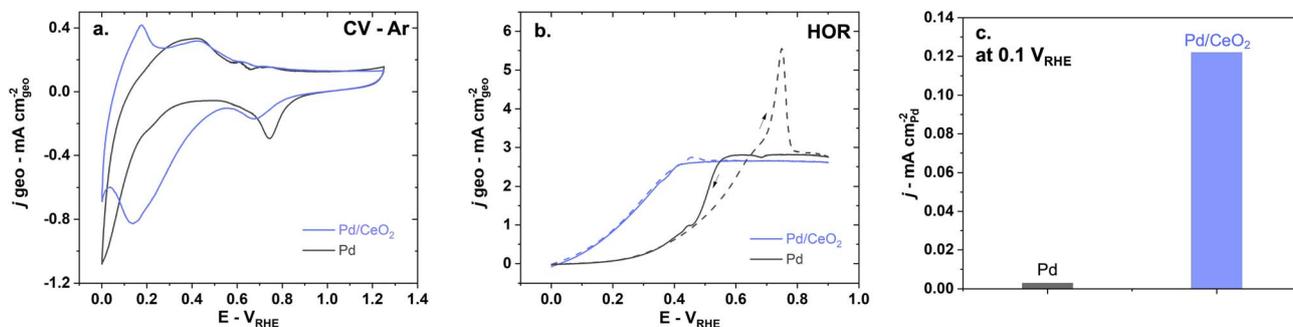
Fig. 2 The presence of CeO$_2$ has a significant impact on hydrogen and oxygen interactions with Pd and leads to better HOR performance as shown in (a) CV at a 50 mV s^{-1} scan rate in Ar-saturated 0.1 M KOH, (b) HOR performed in H$_2$-saturated 0.1 M KOH at 5 mV s^{-1} and 1600 rpm and (c) comparison of specific activity at 0.1 V$_{RHE}$ on pure Pd (black) and Pd/CeO$_2$ (blue).

16374 | *J. Mater. Chem. A*, 2023, **11**, 16370–16382

This journal is © The Royal Society of Chemistry 2023
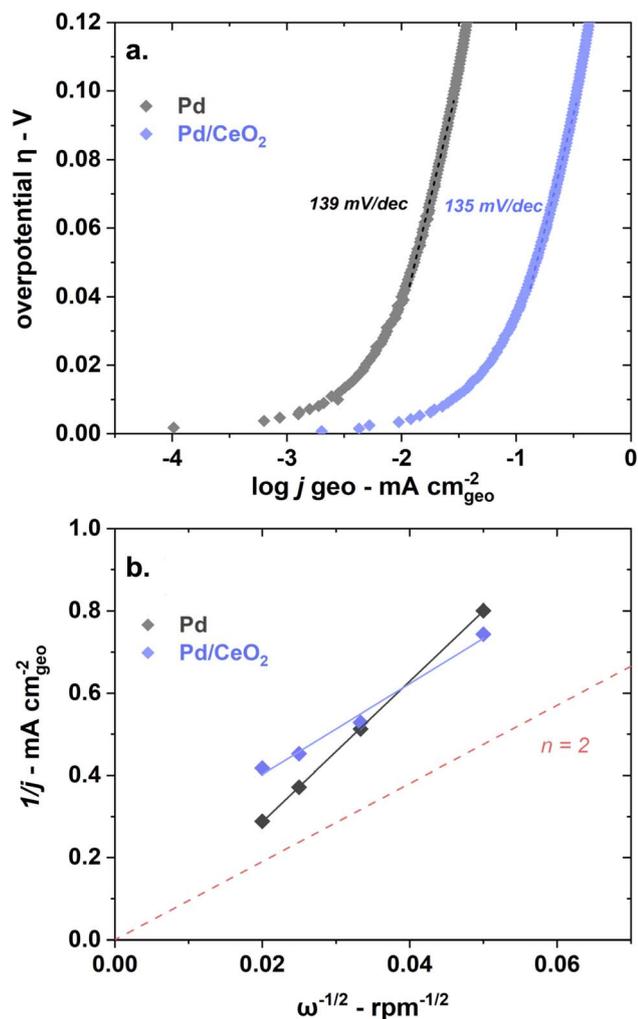
Fig. 3 Pd and Pd/CeO$_2$ show similar Tafel slopes but different estimated number of transferred electrons as shown in (a) a Tafel plot obtained at 5 mV s^{-1} and 1600 rpm and (b) Koutecky–Levich plot obtained at 0.8 V$_{RHE}$ with measurements at 400, 900, 1600 and 2500 rpm at 50 mV s^{-1}. Both reactions were performed in H$_2$-saturated 0.1 M KOH.

with the one obtained on the glassy-carbon electrodes (Fig. S1a†). The scan rate was decreased to 5 mV s^{-1} in the following experiments to better capture mass changes. The ECSA obtained from the integration of charge of Pd oxide reduction before reaction is very similar for Pd and Pd/CeO$_2$ thin films (Table S1†). The frequency changes were thus not corrected for ECSA and were plotted as measured for clarity purposes.

Importantly, the dissipation is the same at the beginning and at the end of the CVs for both Pd and Pd/CeO$_2$ during conditioning and HOR (Fig. S2†). During conditioning in Ar and during HOR, small variations in the dissipation was noticed during the cycles, but the start and end points were similar. This further establishes that (i) the observed changes are solely related to mass changes and (ii) the surface roughness is not significantly affected during cycles.

No measurable metal dissolution occurs on pure Pd thin films in alkaline media in the potential window studied here. The frequency changes were measured as a function of the potential in an Ar-saturated 0.1 M KOH solution (Fig. 4a). These frequency changes appear reversible as the frequency at the beginning of the cycle at ∼0 V$_{RHE}$ is the same after the cycling is completed. This is indicative of a stable thin film with no Pd dissolution. The reversibility of the changes also demonstrate that the entire oxygen–hydrogen potential region is encompassed in this measurement. This contrasts with previous QCM studies showing significant Pd dissolution in acidic solution.[48]

The changes in frequency during the CV can be described in several steps (Fig. 4b):

(1) Hydrogen desorption/oxidation processes lead to an increase in frequency – corresponding to a mass loss – during the anodic scan until ∼0.3 V$_{RHE}$.

(2) Water physisorption/adsorption processes starting at ∼0.3 V$_{RHE}$ until ∼0.75 V$_{RHE}$ lead to a decrease in frequency – corresponding to a mass gain.[49] This is also commonly referred to as the double layer region.
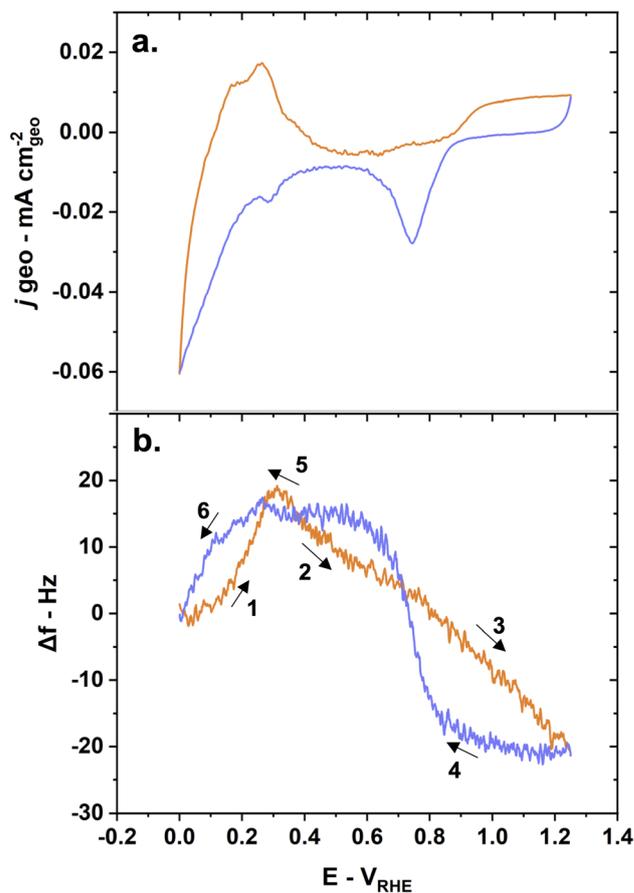
Fig. 4 Mass changes due to hydrogen adsorption, absorption, and desorption behaviors induce frequency changes on pure Pd crystals during conditioning as shown by (a) CV and (b) E-QCM measurements with anodic scans in orange and cathodic scans in blue. Reaction conditions: 5 mV s^{-1} scan rate, Ar-saturated 0.1 M KOH solution.

This journal is © The Royal Society of Chemistry 2023

J. Mater. Chem. A, 2023, **11**, 16370–16382 | **16375**

(3) OH adsorption and subsequent chemisorbed oxide layer formation leads to a continuing decrease in frequency – corresponding to a mass again – until the inversion potential (1.25 V_{RHE}).

(4) Pd oxide layer reduction leads to a drastic increase in frequency – corresponding to a mass loss – at ~0.9 V_{RHE} during the cathodic scan.

(5) Hydrogen adsorption leads to a small increase in frequency – corresponding to a mass loss – at around 0.3 V_{RHE}. This counter intuitive mass loss is due to the displacement of adsorbed water and hydroxyl groups by lighter hydrogen atoms.

(6) Hydrogen absorption leads a drastic decrease in frequency – corresponding to a mass gain and the formation of Pd hydride – starting from 0.3 V_{RHE} until 0 V_{RHE}.

Interestingly, the frequency changes on Pd/CeO$_2$ as a function of the potential show drastic differences compared to pure Pd. With CeO$_2$ as a support for Pd, the changes in frequency are slightly irreversible (Fig. 5b). The difference in frequency at the beginning and end of the cycle is however only less than 5 Hz – corresponding to <10 ng cm^{-2} (using eqn (5)). Possible dissolution of Pd could be an explanation for this small change. A complementary study comparing E-QCM measurements with varying inversion potentials would give further insight into the effect of Pd distribution and oxidation states on stability, but is beyond the scope of this work.[28] It should be noted here that the control sample made of 2 nm of Pd on a 20 nm Ti film (without

CeO$_2$) were not stable and degraded during CV, making a comparison impossible.

On CeO$_2$ alone, the frequency changes can be largely attributed to adsorption and desorption of hydroxyl groups as well as oxidation-reduction of ceria (Fig. 5a and b). The frequency decreases drastically from 0.2 V_{RHE} until 0.8 V_{RHE}. This could correspond to a significant mass increase related to possible oxidation to Ce^{4+} and OH uptake. The small changes in current densities observed at higher potentials are contributions from the Au layer used to promote conductivity. When the potential is decreased, the frequency is constant until ~0.5 V_{RHE}. From 0.5 V_{RHE} until 0.2 V_{RHE}, the frequency increases back to its starting point. This would correspond to a mass loss, related to the possible reduction to Ce^{3+} and desorption of hydroxyl groups from ceria.

The mass changes measured on Pd/CeO$_2$ are dominated by the oxidation/reduction of ceria and adsorption/desorption of hydroxyl groups (Fig. 5c and d). The various steps occurring on pure Pd can also be observed on Pd/CeO$_2$ but there are both minor and major differences:

(1) Hydrogen desorption/oxidation processes lead to an increase in frequency – corresponding to a mass loss – during the anodic scan until ~0.1 V_{RHE}. That represents a ~0.2 V_{RHE} negative shift compared to pure Pd. This is consistent with the shift in the desorption/oxidation current peak observed on the CV obtained on both the glassy carbon electrode (Fig. 2a) and
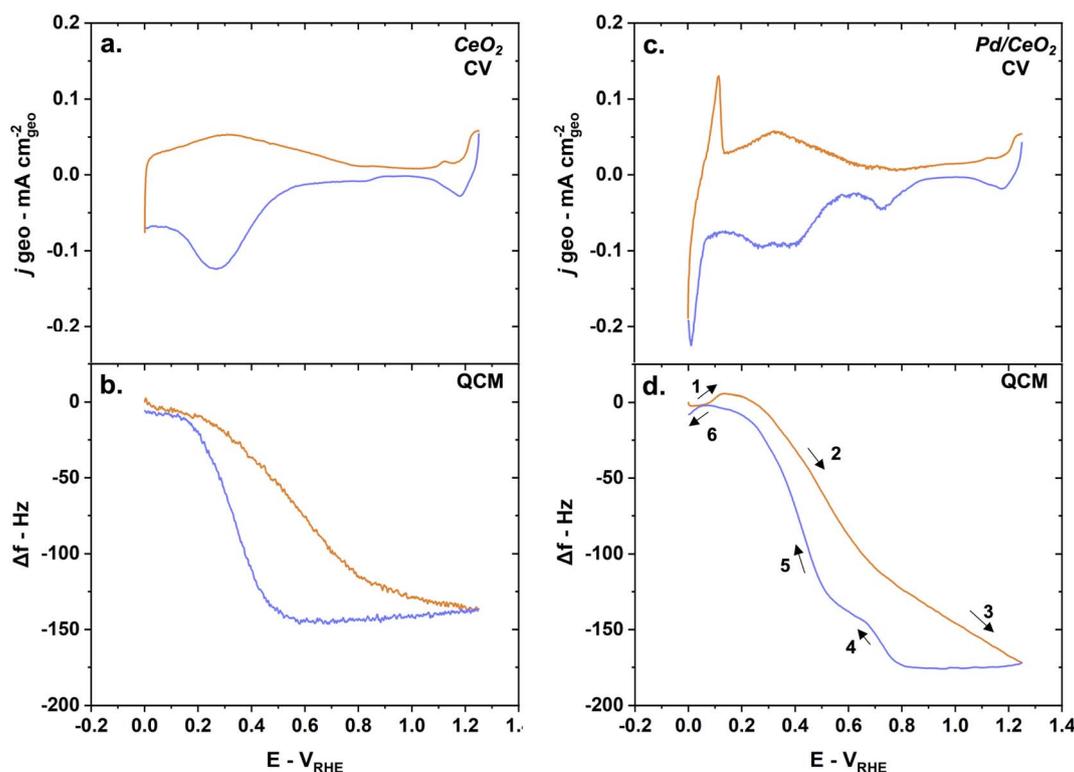
Fig. 5 The mass changes measured on Pd/CeO$_2$ are dominated by adsorption and desorption phenomena occurring on CeO$_2$ during conditioning as shown by (a) CV on CeO$_2$ and simultaneous (b) QCM measurements and (c) CV on Pd/CeO$_2$ and simultaneous (d) QCM measurements. The anodic scans are represented in orange while the cathodic scans are in blue. Reaction conditions: 5 mV s^{-1} scan rate, Ar-saturated 0.1 M KOH solution.

16376 | J. Mater. Chem. A, 2023, **11**, 16370–16382

This journal is © The Royal Society of Chemistry 2023

quartz crystal (Fig. 5c). The increase in frequency is only 6–7 Hz compared to 16–17 Hz on pure Pd, meaning that there is less absorbed hydrogen on Pd/CeO_2 compared to Pd, which is to be expected due to the difference in thicknesses in Pd (2 nm vs. 20 nm).

(2) Oxidation of ceria to Ce^{4+} and adsorption of OH groups lead to a decrease in frequency starting at ~ 0.1 V_{RHE} corresponding to a significant mass gain (Fig. 5d).

(3) Chemisorbed oxide layer formation on Pd leads to a continuing decrease in frequency – corresponding to a mass again – until the inversion potential (1.25 V_{RHE}), as was observed on pure Pd. This significant mass gain is not observed on pure CeO_2 (Fig. 5d) which confirms that this additional mass gain is related to the Pd oxide species.

(4) Pd oxide layer reduction leads to a drastic increase in frequency – corresponding to a mass loss – at ~ 0.8 V_{RHE} during the cathodic scan. This is consistent with the negative shift in Pd oxide reduction potentials observed on the glassy-carbon electrodes (Fig. 2a) and quartz crystals (Fig. 5c).

(5) Desorption and reduction processes lead to a significant increase in frequency – corresponding to a mass loss – starting at around 0.6 V_{RHE}.

(6) Hydrogen absorption leads a small decrease in frequency – corresponding to a small mass gain – starting from 0.05 V_{RHE} until 0 V_{RHE}. The difference is only ~ 5–6 Hz which is consistent with step 1 and corresponds to Pd hydride formation.

An important observation is that during conditioning, the increase in frequency associated with Pd oxides reduction in pure Pd is 35 Hz which corresponds to a mass loss of ~ 69 ng cm_{geo}^{-2}. This is very similar to the frequency changes associated with the reduction of Pd oxides on Pd/CeO_2 of 32 Hz which corresponds to a mass loss of ~ 63 ng cm_{geo}^{-2}. This is consistent with the fact that the two thin films have similar $ECSA_{Pd}$ (Table S1†).

One of the other major observations from these sets of measurements during conditioning in Ar is that in an inert gas environment, OH adsorption processes and oxidation/reduction on CeO_2 are not affected by the presence of Pd. The increase in frequency starting at 0.6 V_{RHE} on negative scans is approximately the same on Pd/CeO_2 and CeO_2. The frequency increases of about 145 Hz in both cases. Considering a surface roughness of *ca.* 1.5 (derived from the ECSA in Table S1†), a Δf of 145 Hz would correspond to a Δm of 285 ng cm_{geo}^{-2}. With a calculated Ce surface density of 7.7×10^{14} of Ce atoms per cm^2, this would give a O/Ce ratio of 9, supporting the hypothesis that a bulk process could also be occurring (*i.e.* reduction). This increase is thus mostly related to OH desorption from the CeO_2 support and reduction of ceria to Ce^{3+}.

New insights from E-QCM during HOR

E-QCM measurements give critical insights into the major differences between Pd and Pd/CeO_2 during HOR. The CV obtained with a scan rate of 5 mV s^{-1} during HOR in H_2-saturated solution while measuring the frequency changes are consistent with the one obtained on glassy-carbon electrodes (Fig. 2a, b, 6a

and c). Pure Pd thin films show poor HOR activity while Pd/CeO_2 shows significant enhancement in activity (Fig. 6a and c).

On pure Pd thin films, mass changes are dominated by the presence of absorbed hydrogen while on Pd/CeO_2 they are dominated by the oxidation/reduction of ceria and adsorption of hydroxyl groups. Indeed, the frequency changes as a function of the potential vary greatly between the two samples during HOR (Fig. 6b and d). On Pd thin films, the frequency increases as the potential increases in the anodic scan (Fig. 6b). This corresponds to a mass loss due to the desorption of absorbed hydrogen in the Pd bulk and its subsequent oxidation to form water. It should be noted here that pure Pd thin films deposited on a Au layer gave similar E-QCM response (Fig. S4†). On Pd/CeO_2 the frequency decreases as the potential increases in the anodic scan (Fig. 6d). This corresponds to a mass gain due to the desorption/oxidation of adsorbed hydrogen on the Pd surface, hydroxyl adsorption and oxidation of ceria to Ce^{4+}. During the cathodic scans, the processes are reversed to reach their initial state. A decrease in frequency is observed on pure Pd (Fig. 6b), corresponding to a mass gain as hydrogen atoms are re-incorporated and absorbed into Pd bulk. In contrast, an increase in frequency is observed on Pd/CeO_2 (Fig. 6d), corresponding to a mass loss due to the displacement of adsorbed hydroxyl groups, reduction of ceria to Ce^{3+} and adsorption of hydrogen atoms on the Pd surface.

E-QCM measurement on CeO_2 during HOR suggests that the adsorbed OH on CeO_2 in Pd/CeO_2 could indeed participate in the HOR (Fig. 7). When comparing the frequency changes on CeO_2 and Pd/CeO_2, there is a difference of ~ 55 Hz corresponding to ~ 108 ng cm_{geo}^{-2} or ~ 73 ng cm_{Pd}^{-2} during HOR (Fig. 7). We propose that this unaccounted mass could correspond to the reaction of OH intermediates on CeO_2 in close contact with adsorbed H on Pd which supports the hypothesis that Pd at the interface with CeO_2 is the active site. We argue that if CeO_2 played no part in the reaction, the mass increase associated with OH adsorption processes and oxidation of ceria during HOR would be similar on both CeO_2 and Pd/CeO_2 just like during conditioning (Fig. 5b and d).

Pd is well dispersed on CeO_2 as shown by HR-TEM

Strong interactions between Pd and CeO_2 on Pd/CeO_2 are observed with TEM (Fig. 8). The Pd thickness (2 nm) was chosen to yield a good dispersion and close interaction of Pd while avoiding a full coverage of the CeO_2 film. The TEM images confirm that such close interaction was achieved. The surface appears homogeneous and presents two types of regions – both containing Pd and CeO_2 – but in different ratios: darker regions are associated with Ce-rich domains and lighter regions with Pd-rich domains. The presence of Pd and CeO_2 phases is confirmed with the fast Fourier transform (FFT) analysis (Fig. 8c). The semi-oriented diffraction pattern rings are consistent with Pd (2.3 Å (111), 1.9 Å (200)) and CeO_2 (3 Å (111), 1.9 Å (220), 1.6 Å (311)). The presence of the CeO_2 phase on Pd/CeO_2 before and after reaction is also confirmed by WAXS (Fig. S5†).

This journal is © The Royal Society of Chemistry 2023

J. Mater. Chem. A, 2023, **11**, 16370–16382 | **16377**
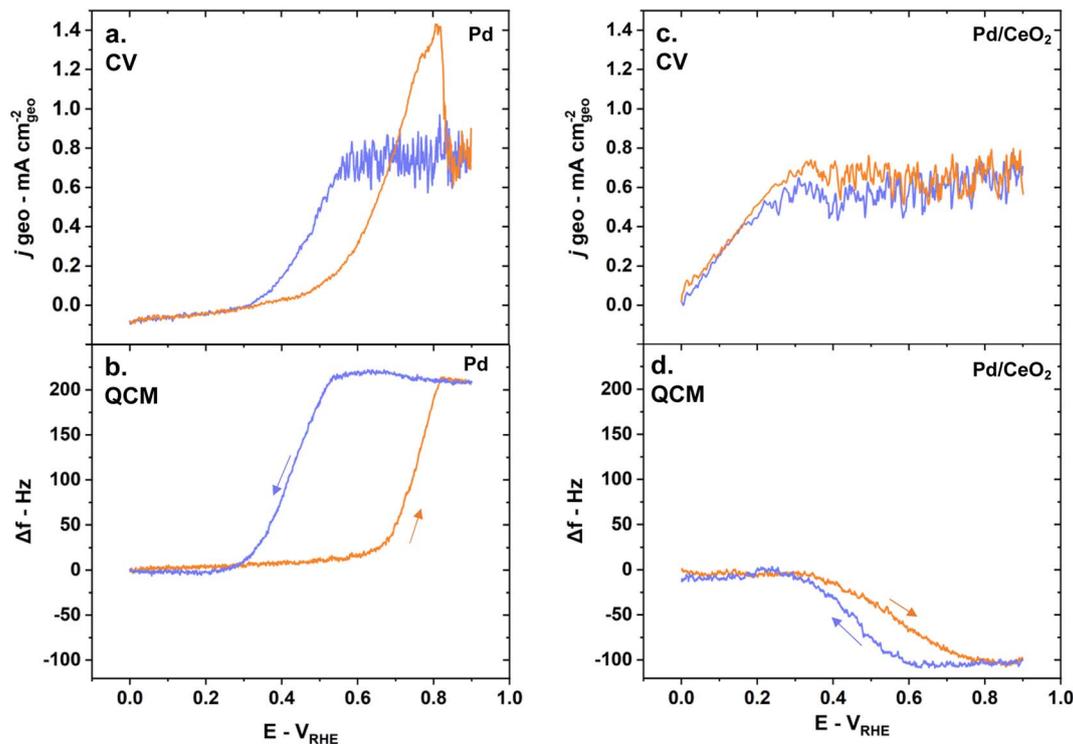
Fig. 6 E-QCM reveals fundamental differences during HOR on Pd and Pd/CeO₂ as shown by (a) the measured current density during CV and (b) simultaneous E-QCM measurements on pure Pd; (c) measured current density during CV and (d) simultaneous E-QCM measurements on Pd/CeO₂. The anodic scans are represented in orange and the cathodic scans in blue. Reaction conditions: 5 mV s⁻¹ scan rate, H₂-saturated 0.1 M KOH solution.
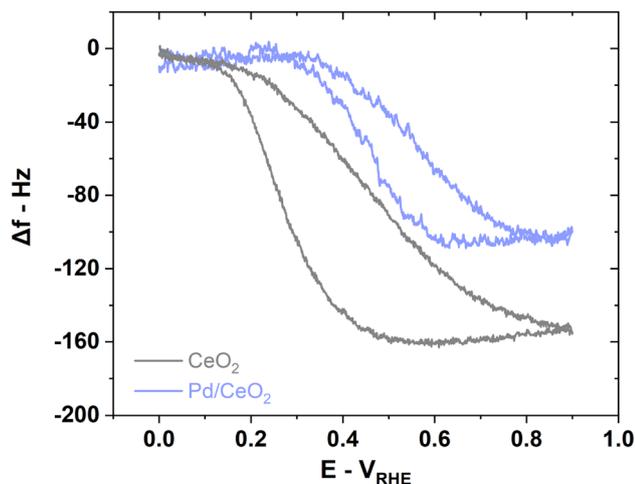
Fig. 7 EQCM measurements on pure CeO₂ reveals the role played by the support on Pd/CeO₂ represented by the difference in frequency during HOR. Reaction conditions: 5 mV s⁻¹ scan rate, H₂-saturated 0.1 M KOH solution.

Strong metal–support interactions are identified with *ex situ* XPS

On pure Pd thin films, surface Pd is in its metallic state before reaction even though Pd is prone to oxidation when exposed to air and ambient conditions (Fig. 9a). The binding energy of Pd $3d_{5/2}$ is 335 ± 0.1 eV as determined by *ex situ* XPS before

reaction. This is consistent with metallic Pd binding energies reported in previous surface studies.[50]

The Pd 3d region of Pd/CeO₂ measured by XPS indicates that there are multiple Pd species with different oxidation states before reaction (Fig. 9b). At least three different contributions could be identified after fitting: a first species at 334.8 ± 0.1 eV (referred to as Pd⁰), a second at 336 ± 0.1 eV (Pd–O), and a third at 337.5 ± 0.1 eV (Pd–O–Ce). This is consistent with previous studies of Pd single atoms dispersed and covalently bonded to CeO₂.[8,51] This confirms that an important fraction of Pd is in close interaction with Ce. XPS measurements alone can however not fully describe all possible Pd species and theoretical insight from calculations of Pd 3d core level shifts are needed (see section below).

After reaction, Pd remains metallic in pure Pd while Pd/CeO₂ still presents at least three main species but with different ratios compared to the fresh sample (Fig. 9c and d). There is a decrease in the metallic Pd⁰ fraction after reaction on Pd/CeO₂: from 55% on the fresh sample to 38% on the used sample (Fig. 9d, Table S3†).

As expected from E-QCM, CV and HOR conditions appear to influence the oxidation state of Ce in Pd/CeO₂ thin films. The ceria support consists mostly of Ce⁴⁺ species before reaction as measured by XPS (Fig. S3†). The uncertainty in the background and noise of the Ce 3d region renders a quantitative analysis of the fresh sample difficult. After reaction, a clear contribution from Ce³⁺ can be measured. This suggests that reduction/

16378 | *J. Mater. Chem. A*, 2023, **11**, 16370–16382

This journal is © The Royal Society of Chemistry 2023
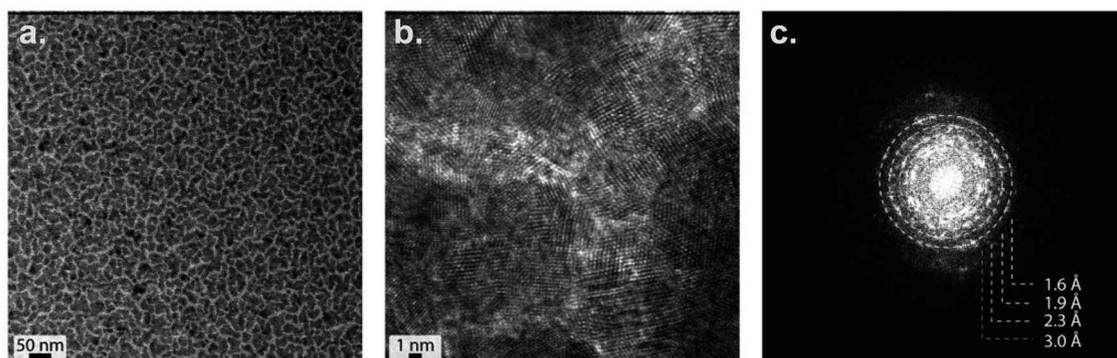
Fig. 8 Close interactions between Pd and CeO$_2$ are observed on TEM images with lighter areas corresponding to Pd rich domains while darker areas can be attributed to Ce-rich domains as shown on (a) and (b) TEM images and (c) FFT analysis.
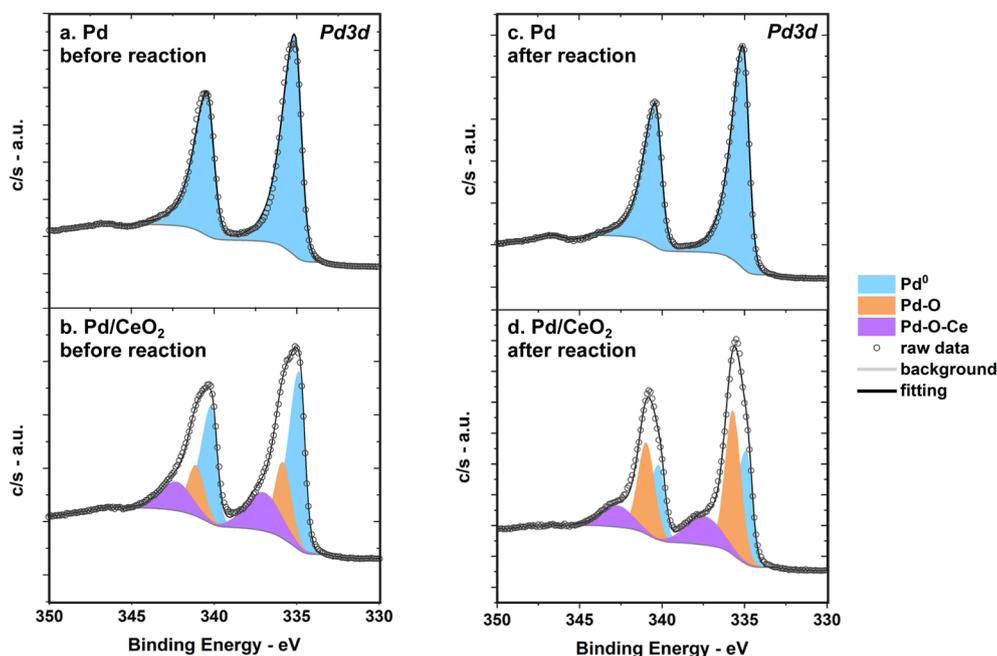
Fig. 9 XPS spectra measured before and after reaction show that Pd remains metallic on pure Pd thin films while Pd is partly oxidized on Pd/CeO$_2$ as shown by the Pd 3d region of pure Pd (a) before reaction and (c) after reaction, and the Pd 3d region of Pd/CeO$_2$ (b) before reaction and (d) after reaction.

oxidation of ceria indeed occur during cycling in HOR. The elemental composition of the Pd/CeO$_2$ sample was also investigated with XPS. It should be noted that the Pd 3d$_{5/2}$/Ce 3d area ratio decreases after reaction (Table S3†), which is consistent with the slight irreversibility of the frequency changes observed during E-QCM (Fig. 4). This would further support the hypothesis that slight dissolution of Pd occurs on Pd/CeO$_2$ during experiment.

Calculated Pd 3d core level shifts

A set of DFT calculations was performed to facilitate the interpretation of the measured Pd 3d binding energies. The considered structures on CeO$_2$(111) are (a) a Pd atom embedded in the top layer of the surface, (b) a Pd ad-atom on the surface,

(c) a small Pd$_7$O$_8$ cluster adsorbed on the surface and (d) a small Pd$_4$ cluster with one atom embedded in the surface (Fig. 10). The structures are chosen to represent different possibilities that have been discussed in the literature for single atoms and small clusters on CeO$_2$(111).

The Pd 3d binding energy is sensitive to the chemical state of the metal. The shift in binding energy is calculated here with respect to the binding energy in PdO by considering a unit cell with three layers of CeO$_2$(111) including the explored Pd structure and three layers of PdO(101). A four-fold Pd atom in the top layer of PdO(101) is used as the reference atom. The computed shift is in this approach converged within about 0.1 eV as compared to bulk PdO.[52] The size of the surface cell is determined by the computed lattice constant for CeO$_2$, which is

This journal is © The Royal Society of Chemistry 2023

J. Mater. Chem. A, 2023, **11**, 16370–16382 | **16379**
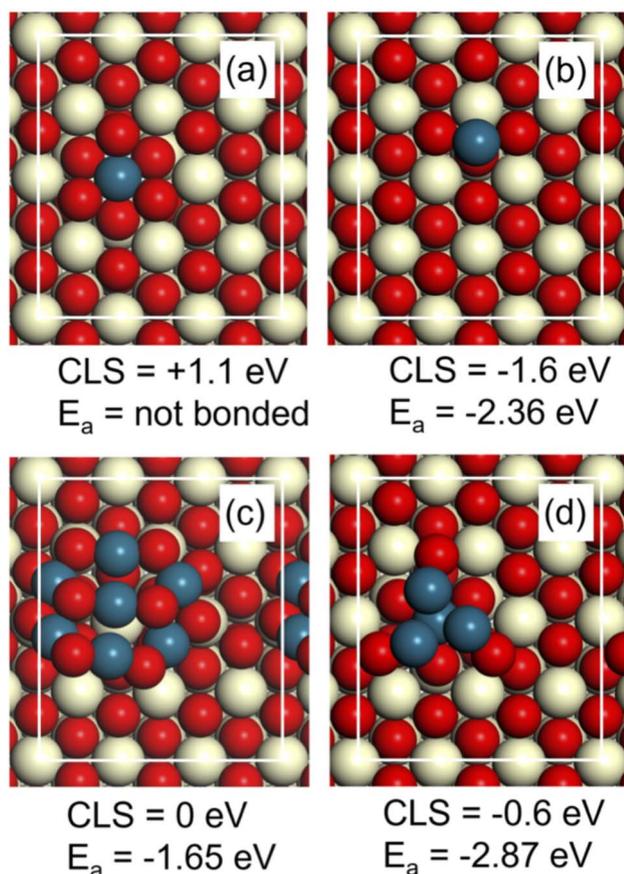
Fig. 10 The considered Pd-structures on $CeO_2(111)$ have significant differences in Pd 3d core level shifts (CLS) and CO adsorption energy (E_a). (a) Pd atom embedded in the top layer, (b) Pd atom adsorbed on the surface, (c) Pd_7O_8 cluster, (d) Pd_4 cluster with one atom embedded in the surface. The Pd 3d CLS are calculated with respect to PdO. Atomic color code: oxygen (red), palladium (blue) and cerium (beige).

5.49 Å. Using the lattice constant of CeO_2, implies that the PdO slab is strained by 8% tensile strain in one direction and 7% compressive strain in the other direction. Test for structure (a) using instead the lattice constant of PdO for the surface cell altered the core level shift by less than 0.1 eV.

The Pd atom embedded in the top layer of the surface (a) has a shift of +1.1 eV with respect to PdO (Fig. 10). A Pd ad-atom (b) has instead a shift of −1.6 eV with respect to PdO. The oxide cluster (c) has on average a shift similar to PdO and the small Pd_4 cluster has a negative shift of −0.6 eV (Fig. 10). In this case, it is the three atoms not embedded in the surface that have a negative shift, whereas the embedded atom has zero shift with respect to PdO. The calculated shifts indicate that the measured value at 337.5 eV in Fig. 9 could be attributed to Pd embedded in CeO_2 (a). It is only embedded Pd that has a substantial positive shift with respect to PdO. The large shift is consistent with a higher charging of Pd as corroborated by a Bader charge analysis. The initial state charge of the embedded Pd is calculated to be 8.63e, whereas the average charge of Pd in PdO is calculated to be 9.11e. The clear negative shift of a Pd ad-atom

on $CeO_2(111)$ (b) is also consistent with the Bader analysis, which yields the initial state charge of 9.76e.

CO-stripping experiments

CO-stripping voltammetry was carried out three consecutive times on both Pd and Pd/CeO_2 quartz crystals. The first runs were performed immediately after HOR and describe the catalyst post-reaction. Interestingly, the first runs vary greatly compared to the second and third runs on both samples. For the first runs, Pd shows a 40 mV shift to lower potential compared to Pd/CeO_2, indicating more facile CO oxidation (Fig. S7†). This is counter intuitive as ceria is expected to facilitate oxidation of CO.[53] The other runs however present similar onsets and potential peaks for both Pd and Pd/CeO_2, indicating that potential cycling and/or exposure to CO have changed the surface. In the literature, the same stripping onset and peak potential have been observed for nanostructured Pd–CeO_2/C and Pd/C in 2 M KOH[54] and 0.1 M KOH.[3]

Mass loss associated with the oxidation of CO and desorption of CO_2 are consistent with the ECSA calculations on pure Pd thin films. As expected, the mass loss (or increase in frequency) measured with E-QCM occurs at lower potential on the first run for Pd compared to the other runs which is consistent with more facile oxidation (Fig. S7†). Moreover, there is a difference in mass loss of 29.3 and 26.7 ng cm^{-2} between the first and the second run which is consistent with different calculated ECSA by cm_{Pd}^2 (Table S1†). This mass change can be related to a number of CO molecules adsorbed per cm_{Pd}^2. Considering a surface density of $\sim 1.3 \times 10^{15}$ Pd atoms per cm^2 (averaged value of Pd(100) and Pd(111)), this gives a Pd to CO ratio of ~ 2.2. This ratio would translate into a preferred bridged CO adsorption mode, on average. This is consistent with a recent FTIR study showing that after purging CO from the cell with Ar, the main adsorbed species are water through OH bonds and bridged CO.[55] No atop CO was observed after purging in Ar. It should be noted that this FTIR study was performed at 0.4 V_{RHE} and in acidic media which could also affect the binding conformation of CO.

In the case of Pd/CeO_2, the mass loss associated with the oxidation of CO and desorption of CO_2 is lower than expected. The mass loss in the first and second runs is only ~ 13 and ~ 14.5 ng cm_{Pd}^{-2} respectively. Using the same atom density as for extended Pd surfaces gives a Pd to CO ratio of ~ 4.3. This ratio is higher than expected. This is partly due to an overestimation of the surface of density of Pd atoms as the surface density of Pd atoms in Pd/CeO_2 is expected to be lower than on close-packed surfaces. Most importantly, this discrepancy could be due to different adsorption energies of CO on Pd/CeO_2.

The CO adsorption energy was calculated on the different model structures (Fig. 10). The adsorption energy (E_a) on the adatom (b) and the cluster (d) is high, which is consistent with the well-known high reactivity of undercoordinated metal sites such as small clusters. The adsorption energy on the Pd_7O_8 cluster is consistent with the adsorption energy on PdO(101).[52] Importantly, we find that CO does not adsorb on the embedded Pd atom (Fig. 10a). This is consistent with the low adsorption

16380 | *J. Mater. Chem. A*, 2023, **11**, 16370–16382

This journal is © The Royal Society of Chemistry 2023

energy of CO on Pd four-fold coordinated to oxygen, such as in the PdO(100) surface.[56] Thus, embedded Pd has a clear signature in XPS but should not be visible in CO-stripping. It should be noted that the embedded site is, however, active for H_2 dissociation. We find that H_2 dissociates without barrier on embedded Pd in a heterolytic fashion forming PdH and an OH group. The subsequent formation of two OH group is strongly preferred thermodynamically by 3 eV. The results highlight the fact that sites that may be relevant for the considered reaction may not be visible in CO-stripping. Additional research involving calculations of the entire potential energy surface of the reactions is, however, required to make conclusions regarding the activity of the considered sites.

Conclusion

The investigation of well-defined model thin films revealed fundamental differences between Pd and Pd/CeO$_2$ during hydrogen oxidation reaction in alkaline media. Pd/CeO$_2$ led to an expected enhancement in HOR performance compared to pure Pd thin films. By combining electrochemical measurements on glassy carbon electrodes, *in situ* electrochemical characterization with quartz crystal microbalance, microscopy and spectroscopy techniques and theoretical calculations, we were able to give a new insight into the enhanced reactivity of Pd/CeO$_2$ in HOR in alkaline media. Strong interaction between Pd and Ce was confirmed by spectroscopy and theoretical calculations where an important fraction of Pd was found to be embedded in the ceria support. E-QCM measurements enabled an estimation of the large source of hydroxyl intermediates provided by CeO$_2$, supporting the hypothesis that these intermediates could be directly participating in the reaction. This work indicates that the interface between Pd and ceria must be carefully designed to provide synergies and to lead to enhanced reactivity. Finally, this study underlines the importance of model thin films as appropriate tools to study the interface between metal and supports in hydrogen oxidation reaction in alkaline media.

Author contributions

ML and BW designed the study, ML wrote the paper, HG performed the DFT calculations and participated in discussions, LS and GMS prepared the materials, ML ran the electrochemical tests, the E-QCM analyses, performed the XPS study and collected the SEM and AFM images, VS performed the HR-TEM analysis, RM provided help with the preliminary results.

Conflicts of interest

There are no conflicts of interest to declare.

Acknowledgements

References

1 L. Osmieri, L. Pezzolato and S. Specchia, *Curr. Opin. Electrochem.*, 2018, **9**, 240–256.

2 S. Gottesfeld, D. R. Dekel, M. Page, C. Bae, Y. Yan, P. Zelenay and Y. S. Kim, *J. Power Sources*, 2018, **375**, 170–184.

3 R. K. Singh, E. S. Davydova, J. Douglin, A. O. Godoy, H. Tan, M. Bellini, B. J. Allen, J. Jankovic, H. A. Miller, A. C. Alba-Rubio and D. R. Dekel, *Adv. Funct. Mater.*, 2020, **30**, 2002087.

4 M. Bellini, M. V. Pagliaro, A. Lenarda, P. Fornasiero, M. Marelli, C. Evangelisti, M. Innocenti, Q. Jia, S. Mukerjee, J. Jankovic, L. Wang, J. R. Varcoe, C. B. Krishnamurthy, I. Grinberg, E. Davydova, D. R. Dekel, H. A. Miller and F. Vizza, *ACS Appl. Energy Mater.*, 2019, **2**, 4999–5008.

5 T.-J. Wang, F.-M. Li, H. Huang, S.-W. Yin, P. Chen, P.-J. Jin and Y. Chen, *Adv. Funct. Mater.*, 2020, **30**, 2000534.

6 T.-J. Wang, W.-S. Fang, Y.-M. Liu, F.-M. Li, P. Chen and Y. Chen, *J. Energy Chem.*, 2022, **70**, 407–413.

7 H. A. Miller, A. Lavacchi, F. Vizza, M. Marelli, F. D. Benedetto, F. D'Acapito, Y. Paska, M. Page and D. R. Dekel, *Angew. Chem., Int. Ed.*, 2016, **55**, 6004–6007.

8 V. Muravev, G. Spezzati, Y.-Q. Su, A. Parastaev, F.-K. Chiang, A. Longo, C. Escudero, N. Kosinov and E. J. M. Hensen, *Nat. Catal.*, 2021, **4**, 469–478.

9 T. W. v. Deelen, C. H. Mejía and K. P. d. Jong, *Nat. Catal.*, 2019, **2**, 955–970.

10 J. Yang, W. Li, D. Wang and Y. Li, *Adv. Mater.*, 2020, **32**, 2003300.

11 T. Montini, M. Melchionna, M. Monai and P. Fornasiero, *Chem. Rev.*, 2016, **116**, 5987–6041.

12 Q. Wang, K. L. Yeung and M. A. Bañares, *Catal. Today*, 2020, **356**, 141–154.

13 R. J. Gorte, *AIChE J.*, 2010, **56**, 1126–1135.

14 M. Li, X. Wang, K. Liu, H. Sun, D. Sun, K. Huang, Y. Tang, W. Xing, H. Li and G. Fu, 2023, 2302462.

15 X. Wang, Y. Tang, J.-M. Lee and G. Fu, *Chem Catal.*, 2022, **2**, 967–1008.

16 X. Wang, Y. Zhu, H. Li, J.-M. Lee, Y. Tang and G. Fu, *Small Methods*, 2022, **6**, 2200413.

17 N. Acerbi, S. C. E. Tsang, G. Jones, S. Golunski and P. Collier, *Angew. Chem., Int. Ed.*, 2013, **125**, 7891–7895.

18 C. A. Campos-Roldán and N. Alonso-Vante, *Electrochem. Energy Rev.*, 2019, **2**, 312–331.

19 W. Sheng, M. Myint, J. G. Chen and Y. Yan, *Energy Environ. Sci.*, 2013, **6**, 1509.

20 D. Strmcnik, M. Uchimura, C. Wang, R. Subbaraman, N. Danilovic, D. v. d. Vliet, A. P. Paulikas,

This journal is © The Royal Society of Chemistry 2023

J. Mater. Chem. A, 2023, **11**, 16370–16382 | **16381**

V. R. Stamenkovic and N. M. Markovic, *Nat. Chem.*, 2013, **5**, 300–306.

21 J. Li, S. Ghoshal, M. K. Bates, T. E. Miller, V. Davies, E. Stavitski, K. Attenkofer, S. Mukerjee, Z.-F. Ma and Q. Jia, *Angew. Chem., Int. Ed.*, 2017, **56**, 15594.

22 N. M. Markovic and P. N. R. Jr, *Surf. Sci. Rep.*, 2002, **45**, 117–229.

23 G. Montserrat-Siso and B. Wickman, *Electrochim. Acta*, 2022, **420**, 140425.

24 K. Sohlberg, S. T. Pantelides and S. J. Pennycook, *J. Am. Chem. Soc.*, 2001, **132**, 6609–6611.

25 W. Xu, Z. Liu, A. C. Johnston-Peck, S. D. Senanayake, G. Zhou, D. Stacchiola, E. A. Stach and J. A. Rodriguez, *ACS Catal.*, 2013, **3**, 975–984.

26 S. Sahoo, D. R. Dekel, R. Maric and S. P. Alpay, *ACS Catal.*, 2021, **11**, 2561–2571.

27 P. C. K. Vesborg, B. Seger and I. Chorkendorff, *J. Phys. Chem. Lett.*, 2015, **6**, 951–957.

28 L. Strandberg, V. Shokhen, M. Luneau, G. Lindbergh, C. Lagergren and B. Wickman, *ChemElectroChem*, 2022, **9**, e202200591.

29 F. D. Speck, F. S. M. Ali, M. T. Y. Paul, R. K. Singh, T. Böhm, A. Hofer, O. Kasian, S. Thiele, J. Bachmann, D. R. Dekel, T. Kallio and S. Cherevko, *Chem. Mater.*, 2020, **32**, 7716–7724.

30 W. Haynes, in *Handbook of Chemistry and Physics*, CRC Press, 95 edn, 2014.

31 S. A. Tschupp, S. E. Temmel, N. P. Salguero, J. Herranz and T. J. Schmidt, *J. Electrochem. Soc.*, 2017, **164**, E3448–E3456.

32 J. Kankare, *Langmuir*, 2002, **18**, 7092–7094.

33 I. Reviakine, A. N. Morozov and F. F. Rossetti, *J. Appl. Phys.*, 2004, **95**, 7712.

34 B. Wickman, H. Grönbeck, P. Hanarp and B. Kasemo, *J. Electrochem. Soc.*, 2010, **157**, B592.

35 M. Grden, J. Kotowski and A. Czerwinski, *J. Solid State Electrochem.*, 2000, 273–278.

36 S. Henning, J. Herranz and H. A. Gasteiger, *J. Electrochem. Soc.*, 2015, **162**, F178–F189.

37 G. Kresse and J. Hafner, *Phys. Rev. B: Condens. Matter Mater. Phys.*, 1993, **47**, 558.

38 G. Kresse and J. Hafner, *Phys. Rev. B: Condens. Matter Mater. Phys.*, 1993, **49**, 14251.

39 G. Kresse and J. Furthmüller, *Comput. Mater. Sci.*, 1996, **6**, 15.

40 G. Kresse and J. Furthmüller, *Phys. Rev. B: Condens. Matter Mater. Phys.*, 1996, **54**, 11169.

41 A. Posada-Borbon, N. Bosio and H. Grönbeck, *Surf. Sci.*, 2021, **705**, 121761.

42 P. E. Blöchl, *Phys. Rev. B: Condens. Matter Mater. Phys.*, 1994, **50**, 17953.

43 J. P. Perdew, K. Burke and M. Ernzerhof, *Phys. Rev. Lett.*, 1996, **77**, 3865.

44 S. L. Dudarev, G. A. Botton, S. Y. Savrasov, C. J. Humphreys and A. P. Sutton, *Phys. Rev. B: Condens. Matter Mater. Phys.*, 1998, **57**, 1505–1509.

45 M. V. d. Bossche, N. M. Martin, J. Gustafson, C. Hakanoglu, J. Weaver, E. Lundgren and H. Grönbeck, *J. Chem. Phys.*, 2014, **141**, 034706.

46 V. Yarmiayev, M. Alesker, A. Muzikansky, M. Zysler and D. Zitoun, *J. Electrochem. Soc.*, 2019, **166**, F3234.

47 T. Shinagawa, A. T. Garcia-Esparza and K. Takanabe, *Sci. Rep.*, 2015, **5**, 13801.

48 M. Grden, J. Kotowski and A. Czerwinski, *J. Solid State Electrochem.*, 1999, **3**, 348–351.

49 K. Shimazu and H. Kita, *J. Electroanal. Chem.*, 1992, **341**, 361–367.

50 J. Andersen, D. Hennig, E. Lundgren, M. Methfessel, R. Nyholm and M. Scheffler, *Phys. Rev. B*, 1994, **50**, 17525.

51 K. R. Priolkar, P. Bera, P. R. Sarode, M. S. Hegde, S. Emura, R. Kumashiro and N. P. Lalla, *Chem. Mater.*, 2002, **14**, 2120–2128.

52 R. Westerström, M. E. Messing, S. Blomberg, A. Hellman, H. Grönbeck, J. Gustafson, N. M. Martin, O. Balmes, R. v. Rijn, J. N. Andersen, K. Deppert, H. Bluhm, Z. Liu, M. E. Grass, M. Hävecker and E. Lundgren, *Phys. Rev. B: Condens. Matter Mater. Phys.*, 2011, **83**, 115440.

53 G. Spezzati, Y. Su, J. P. Hofmann, A. D. Benavidez, A. T. DeLaRiva, J. McCabe, A. K. Datye and E. J. M. Hensen, *ACS Catal.*, 2017, **7**, 6887–6891.

54 H. A. Miller, M. V. Pagliaro, M. Bellini, F. Bartoli, L. Wang, I. Salam, J. R. Varcoe and F. Vizza, *ACS Appl. Energy Mater.*, 2020, **3**, 10209–10214.

55 A. Winiwarter, M. J. Boyd, S. B. Scott, D. C. Higgins, B. Seger, I. Chorkendorff and T. F. Jaramillo, *ChemElectroChem*, 2021, **8**, 250–256.

56 K. Zorn, S. Giorgio, E. Halwax, C. R. Henry, H. Grönbeck and G. Rupprechter, *J. Phys. Chem. C*, 2011, **115**, 1103–1111.

16382 | *J. Mater. Chem. A*, 2023, **11**, 16370–16382

This journal is © The Royal Society of Chemistry 2023